Journal of Materials Chemistry A

ROYAL SOCIETY OF CHEMISTRY

PAPER

View Article Online
View Journal | View Issue

Cite this: J. Mater. Chem. A, 2023, 11, 5864

Electrochemically robust oxide-supported dendritic Pt and Ir nanoparticles for highly effective polymer electrolyte membrane-unitized regenerative fuel cells†

Young-Jin Ko,‡[a] Hyunchul Kim,‡[ab] Woong Hee Lee,[a] Man Ho Han,[a] Cheoulwoo Oh,[a] Chang Hyuck Choi,[cd] Woong Kim,[b] Jeong Min Baik,[ef] Jae-Young Choi,[ef] Peter Strasser*[g] and Hyung-Suk Oh*[aef]

Polymer electrolyte membrane-unitized regenerative fuel cells (PEM-URFCs) are promising energy storage and conversion systems. However, the dissolution of metal species due to frequent phase transformation and support corrosion at high voltages must be addressed. Herein, we design dendritic Pt (PtND) and Ir (IrND) combined with a robust oxide support (antimony doped tin oxide, ATO) for the oxygen electrode. Under ORR and OER potentials, a PtND–IrND/ATO catalyst produced lower average oxidation states of Pt and Ir than a Pt–Ir/C catalyst. Consequently, the Pt and Ir dissolution of PtND–IrND/ATO derived from the phase transition was significantly less than that of Pt–Ir/C. By investigating the operation factors of the URFC, PtND–IrND/ATO was found to exhibit a high round trip efficiency of 50% at 0.4 A cm^{-2} with enhanced long-term stability. Our study not only reveals the fundamental reversible catalytic properties of dendritic catalysts, but also offers insights into the catalyst design concept for the oxygen electrode of URFCs.

Received 25th October 2022
Accepted 20th February 2023

DOI: 10.1039/d2ta08322a

rsc.li/materials-a

Introduction

As a solution to the problem of greenhouse gas emissions, renewable forms of energy, such as sunlight, wind, wave, and geothermal heat, have been in the spotlight owing to their sustainability and environmental friendliness.[1–3] However, renewable energy cannot be supplied continuously and stably because of severe power fluctuations that depend on natural conditions.[4] Moreover, owing to the imbalance between supply and demand, there is a need for auxiliary energy storage and conversion systems. Accordingly, Li batteries, high-efficiency capacitors, redox flow batteries, and polymer electrolyte membranes (PEMs) utilizing regenerative fuel cells (PEM-URFCs) have been suggested as independent power storage devices.[5,6] Among them, the PEM-URFC is a hydrogen-based energy storage system with high cleanliness compared to other systems. This is a concept for a closed-loop system that can use hydrogen fuel to produce electricity as well as regenerate hydrogen and oxygen gases when connected to an external power source.[7,8] PEM-URFCs can operate alternately in two modes: water electrolysis (WE) and fuel cell (FC).

A bifunctional electrocatalyst is required to sustain these modes. A PEM-URFC comprises a hydrogen electrode for the hydrogen oxidation and hydrogen evolution reactions (HOR/HER) and an oxygen electrode for the oxygen reduction and oxygen evolution reactions (ORR/OER). Most PEM-URFC approaches use bifunctional catalysts composed of Pt and Ir oxides. Various types of materials have been investigated, ranging from Pt–Ir alloys to physical mixtures or composites of Pt and Ir oxides.[9–14] One of the main challenges in employing oxygen electrodes for PEM-URFCs is the stability requirement of the catalyst under harsh conditions, characterized by a change from ORR to OER conditions.[15] Due to the severe electrochemical corrosion of carbon supports under OER conditions, the application of carbon supports to enhance the

[a]Clean Energy Research Center, Korea Institute of Science and Technology, Hwarang-ro 14-gil 5, Seongbuk-gu, Seoul 02792, Republic of Korea. E-mail: hyung-suk.oh@kist.re.kr

[b]Department of Materials Science and Engineering, Korea University, 145 Anam-ro, Seongbuk-gu, Seoul 02841, Republic of Korea

[c]Department of Chemistry, Pohang University of Science and Technology (POSTECH), Pohang 37673, Republic of Korea

[d]Institute for Convergence Research and Education in Advanced Technology (I-CREATE), Yonsei University, Seoul 03722, Republic of Korea

[e]School of Advanced Materials Science & Engineering, Sungkyunkwan University (SKKU), Suwon, 16419, Republic of Korea

[f]KIST-SKKU Carbon-Neutral Research Center, Sungkyunkwan University (SKKU), Suwon 16419, Republic of Korea

[g]Department of Chemistry, Chemical Engineering Division, Technical University Berlin, Berlin 10623, Germany. E-mail: pstrasser@tu-berlin.de

† Electronic supplementary information (ESI) available. See DOI: https://doi.org/10.1039/d2ta08322a

‡ These authors contributed equally to this work.

electrochemical activity and stability is restricted.[16–19] Hence, it is essential to develop electrocatalysts with improved activity and stability.

In this study, we combine our previously introduced dendritic Pt, Ir, and conducting metal oxide supports to suggest suitable bifunctional electrocatalyst concepts for PEM-URFCs. Nanodendrites (NDs) are known to exhibit high catalytic activity because of the rich edges and corner atoms resulting from their dendritic structure.[20–27] In another concept, a conducting metal oxide was used as a support instead of carbon to prevent the aggregation and migration of noble metals and maintain catalytic activities. Since highly active nanoparticles including ND are agglomerated under high overpotential of ORR and OER, support materials are used to prevent agglomeration. However, when the supporter is corroded, the agglomeration of metal species occurs more severely. When an insulator is used as a supporter, the electrical resistance of the catalyst increases and the activity is significantly reduced. Therefore, it is possible to overcome these problems by using a support material that does not cause electrochemical corrosion despite having electrical conductivity. As a conducting metal oxide support, mesoporous antimony tin oxide (ATO), which exhibited the largest specific surface area and electrical conductivity in our previous study, was adopted.[28–30] We prepared and characterized Pt-nanodendrite (PtND) and Ir-nanodendrite (IrND) supported on ATO with a high surface area. The electrocatalytic activity and stability of the PtND–IrND/ATO catalyst were demonstrated using three-electrode and PEM-URFC single-cell experiments. The physical properties were investigated *via* TEM, XRD, and various *in situ* characterizations. Our study reveals that dendritic Pt and Ir supported on ATO constitute an effective concept with significant proven benefits in terms of both activity and stability for PEM-URFCs.

Experimental

Preparation of Sb-doped SnO_2 (ATO) support

A mesoporous ATO support with a large surface area was synthesized using a method reported in a previous study.[30] Briefly, 1.20 g of tetradecylamine (TDA, $CH_3(CH_2)_{13}NH_2$, 95%, Sigma-Aldrich) was blended in 200 mL of an ethanol solution (C_2H_5OH 50 mL, DI water 150 mL) and stirred for 1 h. A Two milliliters of tin tetrachloride ($SnCl_4$, 99.995%, Sigma-Aldrich) and 0.446 g of antimony(III) acetate ($(CH_3CO_2)_3Sb$, 99.99%, Sigma-Aldrich) were dissolved in the prepared TDA solution. After stirring for 1 h, 100 mL of ammonium hydroxide solution (3.0 mmol L^{-1}) was added dropwise to the mixture. The resulting solution was refluxed at 80 °C for 72 h and then cooled to room temperature. To remove the TDA surfactant, the white-yellow precipitate was separated from the solution by centrifugation (8000 rpm, 10 min) and then washed several times in an ethanol solution. The resulting wet sample was transferred to a glass-lined stainless-steel autoclave and hydrothermally treated at 120 °C for 24 h. After the hydrothermal reaction, to remove the excess surfactant, the product was centrifuged and washed in ethanol solution several times. The bright-yellow powder was dried in a freeze dryer and calcined in air at 400 °C for 3 h for crystallization. The overall synthesis mechanism of ATO was described in statement S1.†

Preparation of PtND–IrND/ATO catalyst

For the synthesis of PtND and IrND, 0.01 mmol potassium tetrachloroplatinate(II) (K_2PtCl_4, 99%, Kojima) and dihydrogen hexachloroiridate(IV) hydrate ($H_2IrCl_6 \cdot xH_2O$, 99%, Alfa Aesar) were dissolved in 50 and 100 mM of tetradecyltrimethylammonium bromide (TTAB, ≥99%, Sigma Aldrich) solution, respectively. 15 mM of sodium hydroxide (NaOH, 97%, Sigma Aldrich) was dissolved in both solutions, followed by heating to 70 °C with vigorous stirring for 30 min. Subsequently, ascorbic acid (6 mM) and ice-cold $NaBH_4$ solution (150 mM) were rapidly added to the PtND and IrND solutions under stirring, respectively, and the reaction mixture was maintained at 70 °C for 6 h. The resulting solutions were cooled to room temperature. The products were collected by centrifugation and washed several times by an ethanol solution (volume ratio of 1 : 1). The PtND and IrND nanoparticles were blended in the ethanol solution, and an appropriate amount of synthesized ATO was added to the solution with vigorous stirring. Subsequently, PtND and IrND were supported on an ATO support with ultrasonic dispersion for 1 h and then stirred at room temperature for 24 h. Finally, the PtND–IrND/ATO mixture was filtered and dried in a freeze dryer. The detailed synthesis mechanism of PtND and IrND was described in statement S1.†

Material characterization

The structure of the synthesized PtND–IrND/ATO catalyst was observed by transmission electron microscopy (TEM, FEI Titan 300 keV) and high-angle annular dark-field scanning transmission electron microscopy (HAADF-STEM). The atomic distribution was measured using energy-dispersive X-ray spectroscopy (EDS) mapping. Inductively coupled plasma optical emission spectroscopy (ICP-OES, Agilent ICP-OES 725) was performed after pretreatment in aqua-regia solution using microwaves at 250 °C. Wide-angle X-ray diffraction (XRD; Bruker D8 Advance instrument, Cu Kα radiation) was performed to confirm the crystal structures of Pt, Ir, and ATO. Synchrotron X-ray photoemission spectroscopy (XPS) analysis was performed at the ISISS beamline of the Bessy II synchrotron in Helmholtz Zentrum Berlin (HZB). Pt 4f and Ir 4f XPS spectra were analyzed using kinetic energies of 210 and 550 eV, respectively. The detailed experimental setup has been described in a previous study.[29] The Sn 3d and Sb 3d were analyzed using K-alpha (Thermo Scientific) with a micro-focused X-ray probe. Since the Sb $3d^{3/5}$ peak and the O 1s peak overlapped, the peak was deconvoluted (Fig. S1†). The Sb 3d peaks were analyzed, adopting the specific peak area ratio of 2 : 3 relevant to the spin–orbit splitting. Sb was doped in the form of Sb_2O_5 (540.3 eV) and doping ratio of Sb was calculated as 10 at% ($Sn_{0.9}Sb_{0.1}O_{2.05}$). The X-ray adsorption near-edge structure (XANES) of Pt and Ir L_{III}-edge was performed at the 7T-WLS-1 mySpot beamline in BESSY II of the Helmholtz Zentrum Berlin (HZB). Iridium(IV) oxide (IrO_2, Premion, 99.99%, Alfa Aesar) and platinum(IV) chloride ($PtCl_4$, 99.8%, Sigma-

Aldrich) were used as reference materials. The XANES spectra were calibrated with Pt and Ir foil and then normalized using the program Athena with linear pre-edge and polynomial post-edge background subtracted from the raw data.

Electrochemical measurements

All the electrochemical analyses were conducted in a conventional three-electrode system equipped with a Hg/HgO electrode and Pt mesh as the reference and counter electrodes, respectively. A rotating disk electrode (RDE, Pine Instrument, 0.196 cm^2) was used as the working electrode with a loading density of 20.0 μg_{Pt+Ir} cm^{-2}. The catalyst inks were prepared by blending 5 mg of the catalyst in 2.49 mL of isopropyl alcohol (2.49 mL, ≥99.7%, Sigma-Aldrich), 2.49 mL of DI water, and 20 μL of a Nafion® solution (5 wt%, DuPont).

Electrochemical measurements were performed in a 0.05 M H_2SO_4 solution. The ORR and OER were measured in oxygen- and nitrogen-saturated states, respectively. The electrochemical activity of the synthesized catalysts was measured using linear sweep voltammetry at a scan rate of 5 mV s^{-1} and rotating speed of 1600 rpm. The potential ranges for ORR and OER were 1.2–0.2 V_{RHE} and 1.2–2.0 V_{RHE}, respectively. A thin-layer electrochemical flow cell (EFC) connected to a mass spectrometer (Max 300 LG, Extrel) was used for the DEMS study. The working electrode had an exposed area of 0.196 cm^2, and a Pt mesh was used as the counter electrode, connecting the tangential channel to the main inlet channel. The metal-loading density was kept constant at 10.2 μg_{metal} cm^{-2}. Cyclic Voltammetry (CV) mass spectrometer curves were measured during the OER at a scan rate of 5 mV s^{-1} with four selective channels recording the m/z 32 and 44 simultaneously with the electrochemical measurements. The detailed procedure can be found in a previous study.[29]

URFC single-cell measurement

The membrane electrode assembly (MEA) was prepared using a proton exchange membrane (Nafion 212, Dupont) by the catalyst-coated membrane (CCM) method. The synthesized catalysts and commercial Pt/C (46 wt%, TKK) were used as oxygen and hydrogen electrodes, respectively. Catalyst inks were prepared by ultrasonically dispersing 60 mg of the catalyst in 30 mL of isopropyl alcohol and 400 mg of a 5 wt% Nafion® solution (Sigma-Aldrich), which were sprayed directly onto a Nafion membrane with a geometric area of 5 cm^2. The loading densities of the oxygen and hydrogen electrodes were 1 mg_{Pt+Ir} cm^{-2} and 0.4 mg_{Pt} cm^{-2}, respectively. The CCM was hot pressed at 140 °C for 150 s. The URFC single-cell measurements were performed using a potentiostat (Bio-logic) at an operating cell temperature of 80 °C. In the WE mode, pre-heated DI water was supplied to both sides of the oxygen and hydrogen compartments at a constant flow rate of 1.5 mL min^{-1} without back pressure. In the FC mode, 200 sccm of humidified O_2 and H_2 gases were supplied to the oxygen and hydrogen compartments, respectively. Polarization curves for the WE and FC modes were obtained at a scan rate of 5 mV s^{-1} in potential ranges of 1.2–2.0 V and 1.2–0.3 V, respectively.

Online ICP-MS

The degradation of the Pt–Ir/C and PtND–IrND/ATO catalysts was measured online using an ICP-MS (iCAP RQ, Thermo Fisher Scientific) coupled with an EFC. The EFC was equipped with a U-shaped channel with a diameter of 1 mm and an opening for possible contact with the GC working electrode (disk diameter of 1 mm; GC-3155, EC-Frontier). The catalyst ink was prepared by blending the Pt–Ir/C and PtND–IrND/ATO catalysts (5 mg) in an aqueous solution containing isopropyl alcohol and Nafion®. A thin catalyst layer was prepared by dropping the catalyst ink onto the GC with a targeted total metal loading of 50 μg cm^{-2}. A graphite tube (inner diameter of 1 mm) was used as the counter electrode and placed at the EFC inlet, while the reference electrode was connected to the EFC outlet. An Ar-saturated 0.05 M H_2SO_4 electrolyte was used as the electrolyte because of the solid content limit of the ICP-MS apparatus. The electrolyte was introduced into the EFC at a flow rate of 200 μL min^{-1}. Using a Y-connector, the electrolyte was then mixed with 0.05 M H_2SO_4 containing 5 ppb ^{187}Re as an internal standard. The dissolution signal was tracked online by measuring ^{195}Pt and ^{193}Ir signals against the ^{187}Re signal. The thin film electrode was pretreated by 30 fast CV cycles (200 mV s^{-1}) in the potential range of 0.86–1.86 V_{RHE}, and the mass signal was stabilized for 150 s at 0.86 V_{RHE}. The dissolution of the catalysts was measured using cyclic voltammetry (CV, 1st cycle: 0.86–1.46 V_{RHE}; 2nd: 0.86–1.86 V_{RHE}; and 3rd: 0.86–2.26 V_{RHE}) and chronoamperometry (CA, potential: 1.86 V_{RHE}). The online ICP-MS analysis system with a homemade electrochemical flow cell has been described in a previous report.[31]

Results and discussion

Morphology and structure of PtND–IrND/ATO electrocatalyst

Transmission electron microscopy (HR-TEM) showed that the PtNDs and IrNDs exhibited similar morphologies (Fig. 1a and b). Both the NDs were synthesized using a direct surfactant-mediated method with a strong reducing agent, which led to the rapid formation of a large number of small Pt and Ir seeds. These small seeds were self-assembled to reduce the high surface energy, and a surfactant was used to guide the attachment of the seeds to the dendritic structure. The TEM images revealed that the PtND and IrND showed narrow size ranges of 20–30 nm and 15–20 nm, respectively. The PtNDs and IrNDs were supported on the ATO support up to a metal loading of 20 wt% (Fig. 1c). Since the dendritic shape was similar to the mesoporous structure, the contrast between the NDs and the ATO support could not be clearly distinguished in the TEM images. The PtNDs and IrNDs exhibited comparatively uniform dispersion on the ATO support, which was observed by scanning transmission electron microscopy (STEM) and energy dispersive X-ray spectroscopy (EDS, Fig. 1d).

The XRD results confirmed the long-range order and crystalline structure of the PtNDs and IrNDs. The five major diffraction peaks at 39.7°, 46.2°, 67.5°, 82.4°, and 87.1° were indexed to the (111), (200), (220), (311), and (222) reflections of fcc Pt metal (JCPDS card no. 65-2868), respectively. Similarly,

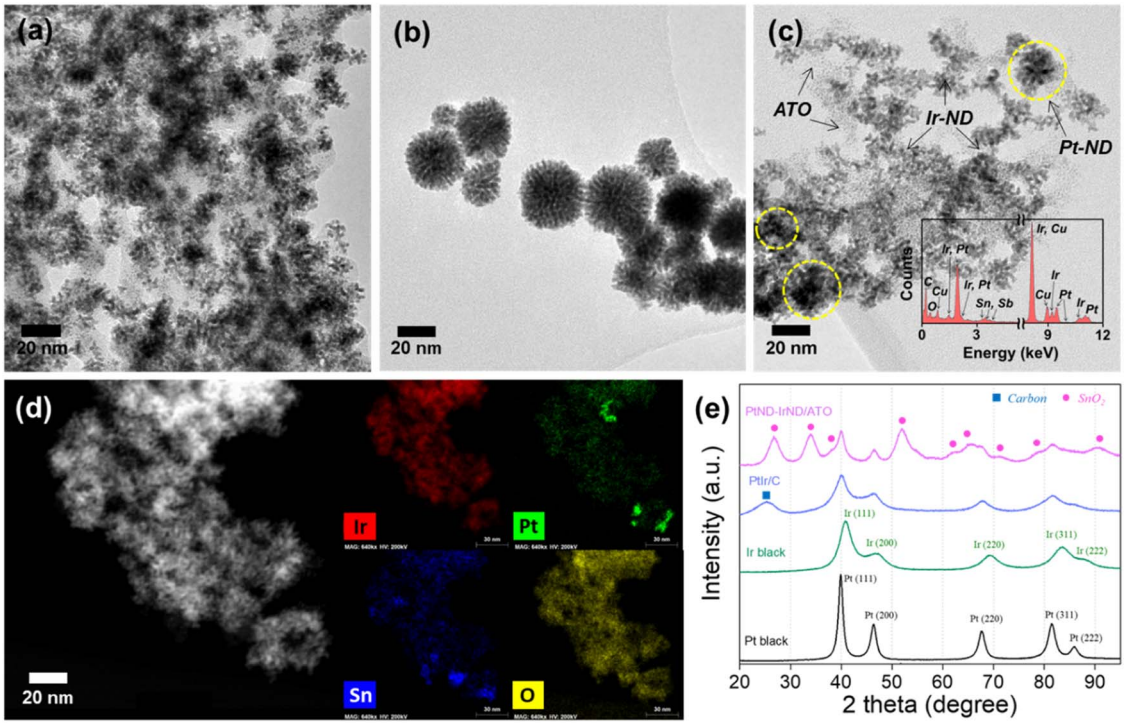

Fig. 1 Morphological and structural characteristics of the synthesized PtND–IrND/ATO catalyst. Low-magnitude TEM images of (a) IrND, (b) PtND, and (c) PtND–IrND/ATO catalyst (inset: EDX pattern of PtND–IrND/ATO catalyst). (d) Representative high-resolution HAADF image and EDX mapping images showing homogeneous Pt and Ir distributions on the ATO support (green: Pt, red: Ir, blue: Sn). (e) Wide-angle XRD patterns of Pt–Ir/C and PtND–IrND/ATO catalysts. Blue square and magenta circle symbols indicate the diffraction patterns of carbon and SnO_2, respectively.

the five major diffraction peaks at 40.6, 47.3, 69.1, 83.4, and 88.2° were indexed to the (111), (200), (220), (311), and (222) reflections of the fcc Ir metal (JCPDS Card no. 87-0715), respectively. Because the reflections of Pt overlapped with those of Ir, we obtained the average particle sizes of Pt and Ir after deconvolution of the (200) reflections. The crystallite size of PtNDs and IrNDs was estimated to be 2.8 nm, respectively. The PtIr/C catalyst was also calculated by the same method using the (220) reflection, and as a result, a particle size of 2.6 nm was obtained (Fig. S2a:† TEM image). The crystalline sizes obtained for Pt black and Ir black were Pt = 4.5 nm and Ir = 3.2 nm, respectively, and only the structure between the catalysts differed (Fig. S2b and c†).

Electrochemical activities of PtND–IrND/ATO electrocatalyst

First, we investigated the ORR activities in O_2-saturated 0.05 M H_2SO_4 solution for the PtND–IrND/ATO catalyst, as shown in Fig. 2a. Rotating disk electrode (RDE) measurements were performed to verify the high ORR activity of the PtND–IrND/ATO catalyst. In the presence of oxygen, the PtND–IrND/ATO catalyst exhibited a high current density polarization curve and a strongly improved overpotential. These results are consistent with those reported in dendrite-related research.[32–35] PtND has more (111) and (311) facets than polycrystalline Pt nanoparticles. The Pt(311) facet is well known as the most active and stable plane for the ORR reaction.[32] In addition, Pt(111) exhibits low oxygen binding energy and high ORR activity, so when reactive intermediates such as O or OH are adsorbed, the Pt site quickly recovers to a clean Pt surface.[32] The Tafel plots of potential *vs.* log j further reveal approximately 60 mV dec^{-1} in the low overpotential region for the RDE experiment, which is consistent with those of Pt-based catalysts (Fig. S3†).[36,37] The behavior of the adsorbed O_2 on the surface of Pt is Temkin isothermal at low overpotentials, with a Tafel slope of 60 mV dec^{-1}.[37] To investigate the kinetic reaction mechanism, we used the Koutecky–Levich plot obtained from the polarization curves at various rotation speeds (Fig. S4 and S5†). In the Koutecky–Levich model, the current density (j) consists of a kinetic current density (j_{kin}) and a diffusion current density (j_{diff}), as shown below:

$$\frac{1}{j} = \frac{1}{j_{kin}} + \frac{1}{j_{diff}} = \frac{1}{j_{kin}} + \frac{1}{B\sqrt{w}}$$

$$B = 0.62nFD_{O_2}{}^{2/3}v^{-1/6}c_{O_2}$$

where D, c, F and V represents the diffusivity, solubility, Faraday constant and kinematic viscosity of the electrolyte, respectively. Based on the Koutecky–Levich model, the number of transferred electrons was calculated to be 3.9 for the PtND–IrND/ATO catalyst, indicating an almost pure four-electron ORR mechanism. Thus, electrochemical measurements in oxygen media

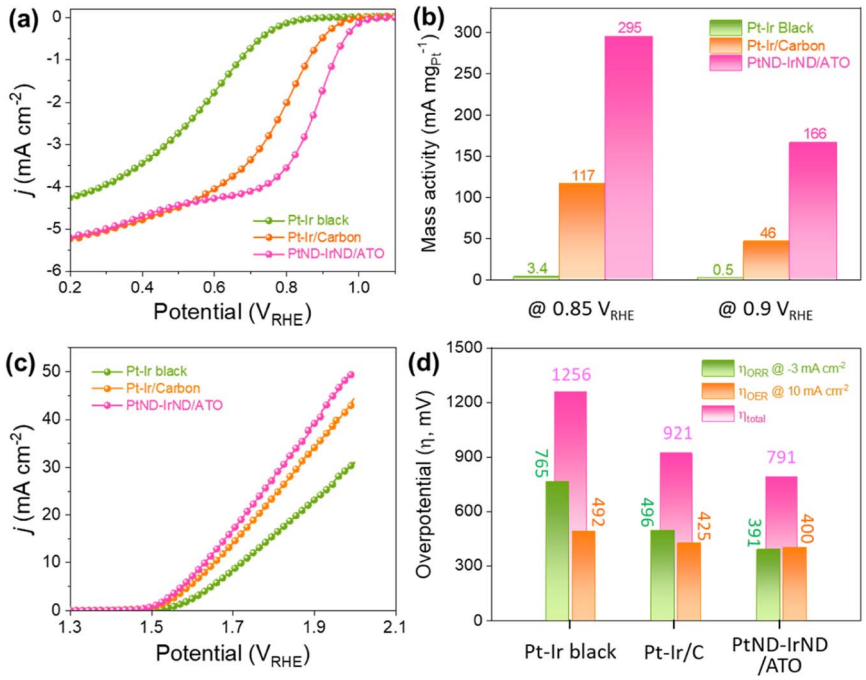

Fig. 2 Electrochemical properties of the synthesized PtND–IrND/ATO catalyst. (a) Electrocatalytic ORR polarization curves and (b) metal-mass based activity at 0.85 and 0.9 V for Pt–Ir black, Pt–Ir/C, and PtND–IrND/ATO catalysts (c) electrocatalytic OER polarization curves for Pt–Ir black, Pt–Ir/C, and PtND–IrND/ATO catalysts. (d) Individual ORR, OER, and total overpotentials for Pt–Ir black, Pt–Ir/C, and PtND–IrND/ATO catalysts.

confirmed the high mass activity of the PtND–IrND/ATO catalyst for the selective reduction of oxygen to water, even in acidic media (Fig. 2b).

Fig. 2c shows the typical polarization curves for the OER on the PtND–IrND/ATO catalyst obtained using RDE measurements. From the polarization curves, the PtND–IrND/ATO catalyst showed slightly higher OER activity than the other catalysts. Fig. 2d exhibits the combined overpotentials of three catalysts in reversible oxygen electrode. The PtND–IrND/ATO catalyst exhibited not only low overpotential in both ORR and OER, but also small overpotential difference between two reactions. The improvement of total overpotential of the PtND–IrND/ATO catalyst compared to Pt–Ir/C catalyst demonstrated the superiority of our catalyst concept.

URFC single-cell performances

To further develop large-scale applications, it is desirable to investigate PEM-URFC single cells that convert water to O_2 and H_2 at oxygen and hydrogen electrodes, respectively. Fig. 3a shows steady-state polarization curves, which are represented as EC and FC performances. Table S1† presents the round-trip efficiency (RT) and cell potential at specific current densities between the EC and FC modes. Although there was no difference in the active surface area of metal species (Fig. S6:† CV of MEAs), the PtND–IrND/ATO catalyst required cell voltages of only 0.747 V and 1.49 V to achieve a current density of 0.5 A cm^{-2} for FCE (fuel-to electrical efficiency: 60.7%) and ECE (electrical-to-fuel efficiency: 82.5%), which are superior to those of state-of-art Pt–Ir catalysts and previously reported heterogeneous catalysts.[41,43–45] It exhibited an RT efficiency of 50% at 0.5 A cm^{-2} and maintained an RT efficiency of nearly 40% at 1 A cm^{-2}. The RT efficiency according to catalyst loading in literature is summarized for an oxygen electrode in the working electrode (Fig. 3b). Most previous studies reported a constant-gas mode, which requires a high metal loading density (>2 $mg_{(Pt+Ir)}$ cm^{-2}) to obtain a high RT (>30%) value at 0.5 A cm^{-2}.[39,40] As shown in this study, in spite of the relatively low concentration of the electrolyte, a high RT of over 50% could be obtained at 0.5 A cm^{-2} using only 1 $mg_{(Pt+Ir)}$ cm^{-2} by adopting the PtND–IrND/ATO catalyst.

Long-term durability tests are indispensable for the commercialization of PEM-URFCs. However, few studies have reported the long-term durability results for PEM-URFCs. Herein, the long-term durability of the PtND–IrND/ATO catalyst was confirmed at 0.5 A cm^{-2} for 48 h at a loading density of 1 $mg_{(Pt+Ir)}$ cm^{-2} (Fig. 3c). The durability test comprised eight cycles of both operations, with each operation performed for 3 h. The PtND–IrND/ATO catalyst exhibited comparable durability in the cyclic test, with potential degradation rates of 1.25 and 2.29 mV h^{-1} for the FC and EC modes, respectively. The initial ORR performance of the PtND–IrND/C catalyst exhibited comparable to that of PtND–IrND/ATO catalyst due to the high conductivity of the carbon supporter, but the performance rapidly decreased in OER due to carbon corrosion (Fig. S7†). Pt–Ir/ATO catalyst showed poor ORR and OER performance due to relatively low conductivity of ATO supporter than those of carbon supporter. This might be attributed to both the high catalytic activities of Pt-ND and Ir-ND with the high corrosion resistance of the conducting oxide support and nanodendritic structure.

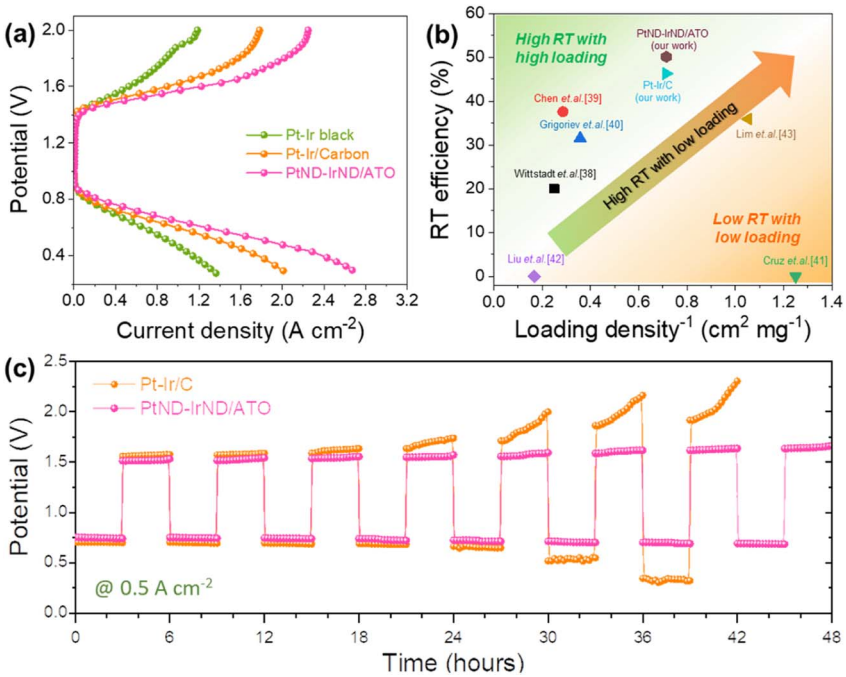

Fig. 3 URFC performances and durability for PtND–IrND/ATO catalyst. (a) URFC performance of Pt–Ir black, Pt–Ir/C, and PtND–IrND/ATO catalysts. (b) Comparison of RT efficiency at 0.5 A cm^{-2} *versus* reciprocal values of the total catalyst loading density (cm^2 mg^{-1}).[38–43] (c) Long-term URFC operation at 0.5 A cm^{-2} during 48 h. Long-term URFC operation comprising eight cycles of both ORR and OER operations, where each operation was performed for 3 h.

Correlation between surface chemistry and catalytic stability

We now investigate how the thicknesses of the Pt and Ir oxide layers depend on the Pt and Ir structures. The oxide thicknesses of ORR and OER catalysts have been previously studied to control the activity and stability of the active catalyst phase.[29] Therefore, we performed synchrotron depth-resolved XPS to apply the Pt–Ir alloy and PtND–IrND catalysts to this theory. The applied kinetic energies of 210 and 550 eV correspond to the inelastic mean free paths of 5.2 and 9.3 Å, respectively, based on the TPP-2M predictive formula.[46] Fig. 4a andb shows the proportion of Pt^0 and Ir^0 with respect to the total intensity (Fig. S8 and S9:† depth-resolved XPS after OER and ORR, respectively). The significant information that can be obtained from depth-resolved XPS is as follows. (1) The PtND–IrND/ATO catalyst exhibited a metallic phase in both Pt and Ir species. (2) The Pt–Ir/C catalyst exhibited a large change in the oxidation state during the ORR and OER. (3) The change in the oxidation state of the metal, which does not participate in the reaction (Ir in ORR or Pt in OER), was also relatively significant in the Pt–Ir/C catalyst. As shown in the XANES spectra for both Pt and Ir, the oxidation state of the PtND–IrND/ATO catalyst was lower than that of the Pt–Ir/C catalyst (Fig. S10†). In particular, in the OER potential, the oxidation state of Ir for the Pt–Ir/C catalyst significantly increased, whereas that of the PtND–IrND/ATO catalyst did not exhibit any significant increase. Because URFC involves repeated OER and ORR operations, there will be differences in the performance and durability of the URFC due to the difference in the phase change depending on the cell potential between the Pt–Ir/C and PtND–IrND/ATO catalysts.

To obtain further information for the faradaic efficiency of the electrocatalysts under OER, differential electrochemical mass spectrometry (DEMS) was performed with a three-electrode system. Along with the electrochemical current, the mass spectrometric signals for oxygen ($m/z = 32$) and carbon dioxide ($m/z = 44$) were recorded. As shown in Fig. 4c, PtND–IrND/ATO catalyst exhibits almost 100% faradaic efficiency for O_2, demonstrating a high selectivity toward OER. However, Pt–Ir/carbon catalyst showed a faradaic efficiency of 85% because of carbon corrosion along with OER; it can be seen that the corrosion of carbon supporter acted as one of the main reasons of the performance degradation in the durability test for Pt–Ir/C catalyst.

To track the reversible reactivity characteristic, *in situ*/operando ICP-MS analysis was performed by changing the applied potential under the reaction conditions (Fig. 4d). *In situ*/operando ICP-MS is a unique technique to reveal real-time electrochemical dissolution, which is driven by direct dissolution and oxygen lattice participation in the ORR and OER. As shown in Fig. 4e, three types of dissolution signals can be observed. First, the peaks of the OER intermediate dissolution observed at the highest potential (Type 1) are indicated by an intermediate metal species during the OER and lattice oxygen participation.[47–50] Second, the peaks of reversible reduction dissolution (Type 2), which are located close to 1.2 V_{RHE}, close to the standard potential of Pt and Ir oxidation reactions, exhibited electrochemical dissolution of reversible metal oxides.[51] Third, the peaks of irreversible reduction dissolution (Type 3) were observed at the lowest potential, representing cathodic

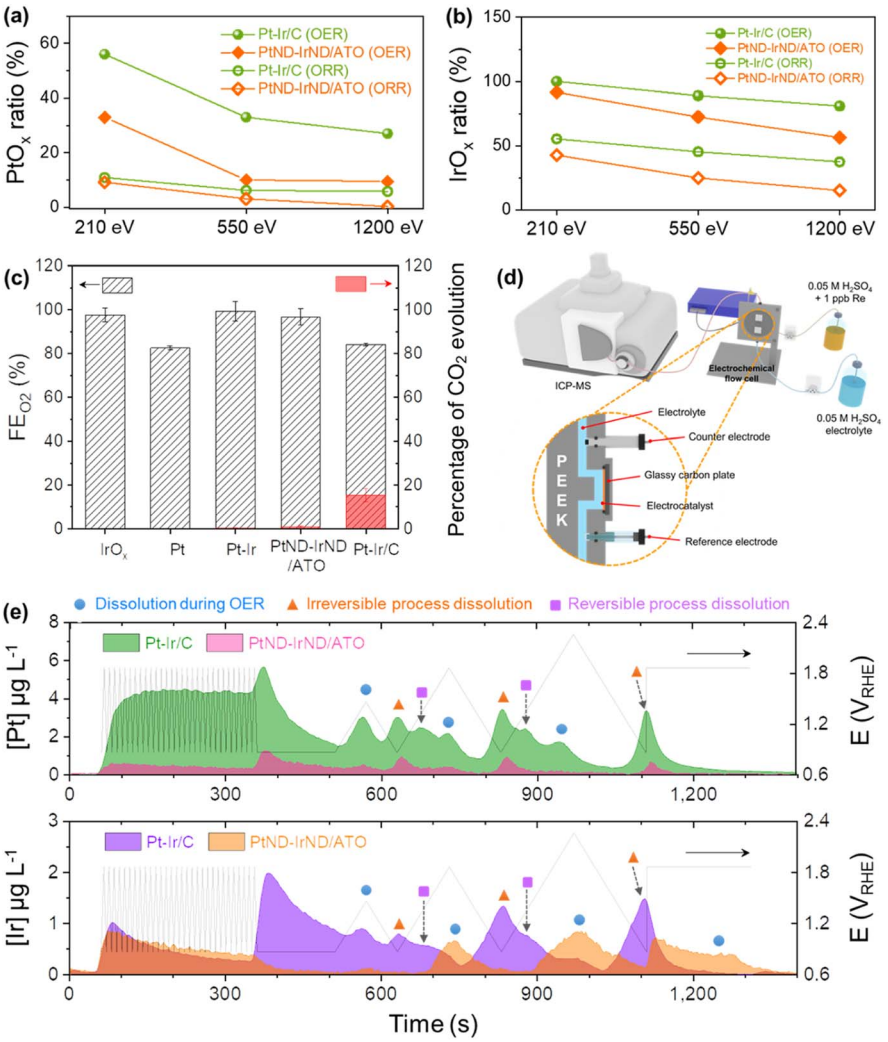

Fig. 4 Stability of Pt and Ir corresponding to its surface chemistry during ORR and OER for synthesized catalysts by depth-resolved XPS and *in situ*/operando ICP-MS. Peak area ratio of (a) Pt oxide and (b) Ir oxide obtained by depth-resolved XPS spectra for Pt–Ir/C and PtND–IrND/ATO catalysts after ORR and OER with different kinetic energies at photoelectron voltages of 210, 550, and 1200 eV. (c) Faradaic efficiency of Pt–Ir black, Pt–Ir/C, and PtND–IrND/ATO catalysts. (d) System of online ICP-MS analysis with homemade electrochemical flow-type device. (e) Real-time Pt and Ir dissolution profiles of Pt–Ir/C and PtND–IrND/ATO catalysts under a representative experimental sequence.

dissolution due to irreversible metal oxides.[48–50] Both the peaks indicate cathodic dissolution of the metal oxide. All the three peaks were lower for the PtND–IrND/ATO catalyst because the Pt/PtO$_x$ redox reaction occurred much less frequently during the ORR and OER. In the case of Ir, type 2 and 3 dissolution occurred significantly for the Pt–Ir/C catalyst, whereas type 1 dissolution occurred for the PtND–IrND/ATO catalyst. The PtND–IrND/ATO catalyst, which maintains a more metallic Ir phase, was dissolved as it was oxidized during the OER, while the Pt–Ir/C catalyst, which has many surfaces oxide phases, caused cathodic dissolution. Because the total dissolution rates of both Pt and Ir were low for the PtND–IrND/ATO catalyst, it was stable during URFC operation. In addition, as shown in Fig. S11,† the dissolution of Sn and Sb hardly occurred during the OER and ORR; since the dissolution of Pt and Ir as well as corrosion of supporter was negligible, only little degradation in performances was occurred for the PtND–IrND/ATO catalyst.

Conclusions

In summary, we present dendritic Pt and Ir supported on an ATO catalyst with high activity and stability, utilized as a catalyst for the oxygen electrode. This catalyst exhibited comparable combined OER/ORR activity in acidic solutions. Lower average oxidation states of Pt and Ir were observed after ORR and OER with the PtND–IrND/ATO catalyst than with the Pt–Ir/C catalyst. In addition, the transformation ratio in the oxidation state was relatively low when the PtND–IrND/ATO catalyst exhibited ORR and OER potentials. Therefore, the dissolution of Pt and Ir derived from the phase transition was significantly lower than that of the Pt–Ir/C catalyst. Beyond the RDE screenings, we further investigated PEM-URFC operations. The PtND–IrND/ATO catalyst exhibited superior RT values with a low catalyst loading. Furthermore, based on our durability test in WE and FC modes, the PtND–IrND/ATO catalyst exhibited high

reversibility for the ORR/OER under single-cell conditions. Our nanocatalyst design concept can impart excellent reversible properties in URFC applications.

Author contributions

Hyung-Suk Oh: conceptualization and supervision. Peter Strasser: writing – review & editing. Young-Jin Ko: investigation and writing – original draft. Hyunchul Kim: investigation. Woong Hee Lee, Man Ho Han, Cheoulwoo Oh, Jeong Min Baik: resource and methology. Chang Hyuck Choi: methology and validation. Woong Kim and Jae-Young Choi: resource.

Conflicts of interest

There are no conflicts to declare.

Acknowledgements

This work was supported by an institutional program grant from the Korea Institute of Science and Technology and the "Carbon to X Project" (Project No. 2020M3H7A1098229) of the National Research Foundation (NRF) funded by the Ministry of Science and ICT, Republic of Korea. This work was also supported by a National Research Council of Science & Technology (NST) grant from the Korean government (MSIP) (No. CAP21011-100), and a National Research Foundation of Korea (NRF) grant funded by the Korean government (MSIT) (NRF-2021R1A2C2093467).

Notes and references

1 C. C. L. McCrory, S. Jung, I. M. Ferrer, S. M. Chatman, J. C. Peters and T. F. Jaramillo, *J. Am. Chem. Soc.*, 2015, **137**, 4347–4357.
2 S. Siracusano, N. Hodnik, P. Jovanovic, F. Ruiz-Zepeda, M. Šala, V. Baglio and A. S. Aricò, *Nano Energy*, 2017, **40**, 618–632.
3 M. Carmo, D. L. Fritz, J. Mergel and D. Stolten, *Int. J. Hydrogen Energy*, 2013, **38**, 4901–4934.
4 T. M. Gür, *Energy Environ. Sci.*, 2018, **11**, 2696–2767.
5 Y. Wang, D. Y. C. Leung, J. Xuan and H. Wang, *Renewable Sustainable Energy Rev.*, 2016, **65**, 961–977.
6 H. Zhong, L. Alberto Estudillo-Wong, Y. Gao, Y. Feng and N. Alonso-Vante, *J. Energy Chem.*, 2021, **59**, 615–625.
7 K. Dutta, D. Rana, H. S. Han and P. P. Kundu, *Fuel Cells*, 2017, **17**, 736–751.
8 Y. N. Regmi, X. Peng, J. C. Fornaciari, M. Wei, D. J. Myers, A. Z. Weber and N. Danilovic, *Energy Environ. Sci.*, 2020, **13**, 2096–2105.
9 T. Ioroi, N. Kitazawa, K. Yasuda, Y. Yamamoto and H. Takenaka, *J. Appl. Electrochem.*, 2001, **31**, 1179–1183.
10 F. Godínez-Salomón, L. Albiter, R. Mendoza-Cruz and C. P. Rhodes, *ACS Appl. Energy Mater.*, 2020, **3**, 2404–2421.
11 J.-H. Kim, S.-W. Yun, K. Shim, S.-H. You, S.-M. Jung, H. Kweon, S. H. Joo, Y. H. Moon and Y.-T. Kim, *ACS Appl. Energy Mater.*, 2020, **3**, 1423–1428.
12 G. C. da Silva, M. R. Fernandes and E. A. Ticianelli, *ACS Catal.*, 2018, **8**, 2081–2092.
13 J. Du, J. Quinson, D. Zhang, F. Bizzotto, A. Zana and M. Arenz, *ACS Catal.*, 2021, **11**, 820–828.
14 S. S. Sekhon, J. Lee and J.-S. Park, *J. Energy Chem.*, 2022, **65**, 149–172.
15 G. C. da Silva, K. J. J. Mayrhofer, E. A. Ticianelli and S. Cherevko, *J. Electrochem. Soc.*, 2018, **165**, F1376–F1384.
16 I. S. Filimonenkov, C. Bouillet, G. Kéranguéven, P. A. Simonov, G. A. Tsirlina and E. R. Savinova, *Electrochim. Acta*, 2019, **321**, 134657.
17 J. Zhao, Z. Tu and S. H. Chan, *J. Power Sources*, 2021, **488**, 229434.
18 L. Castanheira, W. O. Silva, F. H. B. Lima, A. Crisci, L. Dubau and F. Maillard, *ACS Catal.*, 2015, **5**, 2184–2194.
19 K. Kodama, T. Nagai, A. Kuwaki, R. Jinnouchi and Y. Morimoto, *Nat. Nanotechnol.*, 2021, **16**, 140–147.
20 F. Wang, C. Li, L.-D. Sun, C.-H. Xu, J. Wang, J. C. Yu and C.-H. Yan, *Angew. Chem., Int. Ed.*, 2012, **51**, 4872–4876.
21 M. A. Mahmoud, C. E. Tabor, M. A. El-Sayed, Y. Ding and Z. L. Wang, *J. Am. Chem. Soc.*, 2008, **130**, 4590–4591.
22 A. Mohanty, N. Garg and R. Jin, *Angew. Chem., Int. Ed.*, 2010, **49**, 4962–4966.
23 H. Lee, S. E. Habas, S. Kweskin, D. Butcher, G. A. Somorjai and P. Yang, *Angew. Chem., Int. Ed.*, 2006, **45**, 7824–7828.
24 L. Wang and Y. Yamauchi, *J. Am. Chem. Soc.*, 2009, **131**, 9152–9153.
25 B. Lim, M. Jiang, P. H. C. Camargo, E. C. Cho, J. Tao, X. Lu, Y. Zhu and Y. Xia, *Science*, 2009, **324**, 1302–1305.
26 X. X. Zhu, L. Huang, M. Wei, P. Tsiakaras and P. K. Shen, *Appl. Catal., B*, 2021, **281**, 119460.
27 Y. X. Lu, S. F. Du and R. Steinberger-Wilckens, *Appl. Catal., B*, 2016, **199**, 292–314.
28 H. N. Nong, H.-S. Oh, T. Reier, E. Willinger, M.-G. Willinger, V. Petkov, D. Teschner and P. Strasser, *Angew. Chem., Int. Ed.*, 2015, **54**, 2975–2979.
29 H.-S. Oh, H. N. Nong, T. Reier, A. Bergmann, M. Gliech, J. Ferreira de Araújo, E. Willinger, R. Schlögl, D. Teschner and P. Strasser, *J. Am. Chem. Soc.*, 2016, **138**, 12552–12563.
30 H.-S. Oh, H. N. Nong and P. Strasser, *Adv. Funct. Mater.*, 2015, **25**, 1074–1081.
31 W. H. Lee, H. N. Nong, C. H. Choi, K. H. Chae, Y. J. Hwang, B. K. Min, P. Strasser and H.-S. Oh, *Appl. Catal., B*, 2020, **269**, 118820.
32 Y. Jang, K.-H. Choi, D. Y. Chung, J. E. Lee, N. Jung and Y.-E. Sung, *ChemSusChem*, 2017, **10**, 3063–3068.
33 C. Kim, J.-G. Oh, Y.-T. Kim, H. Kim and H. Lee, *Electrochem. Commun.*, 2010, **12**, 1596–1599.
34 H. Kwon, M. K. Kabiraz, J. Park, A. Oh, H. Baik, S.-I. Choi and K. Lee, *Nano Lett.*, 2018, **18**, 2930–2936.
35 S. Ghosh, S. Mondal and C. Retna Raj, *J. Mater. Chem. A*, 2014, **2**, 2233–2239.
36 U. A. Paulus, T. J. Schmidt, H. A. Gasteiger and R. J. Behm, *J. Electroanal. Chem.*, 2001, **495**, 134–145.
37 L. G. R. A. Santos, K. S. Freitas and E. A. Ticianelli, *Electrochim. Acta*, 2009, **54**, 5246–5251.

38 U. Wittstadt, E. Wagner and T. Jungmann, *J. Power Sources*, 2005, **145**, 555–562.
39 G. Chen, H. Zhang, H. Zhong and H. Ma, *Electrochim. Acta*, 2010, **55**, 8801–8807.
40 S. A. Grigoriev, P. Millet, V. I. Porembsky and V. N. Fateev, *Int. J. Hydrogen Energy*, 2011, **36**, 4164–4168.
41 J. C. Cruz, V. Baglio, S. Siracusano, R. Ornelas, L. G. Arriaga, V. Antonucci and A. S. Aricò, *Int. J. Hydrogen Energy*, 2012, **37**, 5508–5517.
42 J. X. Liu, H. Guo, X. M. Yuan, F. Ye and C. F. Ma, *Int. J. Energy Res.*, 2018, **42**, 2823–2834.
43 A. Lim, H.-Y. Jeong, Y. Lim, J. Y. Kim, H. Y. Park, J. H. Jang, Y.-E. Sung, J. M. Kim and H. S. Park, *Sci. Adv.*, 2021, **7**, eabf7866.
44 P. Kúš, A. Ostroverkh, I. Khalakhan, R. Fiala, Y. Kosto, B. Šmíd, Y. Lobko, Y. Yakovlev, J. Nováková, I. Matolínová and V. Matolín, *Int. J. Hydrogen Energy*, 2019, **44**, 16087–16098.
45 P. Gayen, X. Liu, C. He, S. Saha and V. K. Ramani, *Sustainable Energy Fuels*, 2021, **5**, 2734–2746.
46 S. Tanuma, C. J. Powell and D. R. Penn, *Surf. Interface Anal.*, 1994, **21**, 165–176.
47 S. Cherevko, S. Geiger, O. Kasian, A. Mingers and K. J. J. Mayrhofer, *J. Electroanal. Chem.*, 2016, **773**, 69–78.
48 S. Cherevko, S. Geiger, O. Kasian, A. Mingers and K. J. J. Mayrhofer, *J. Electroanal. Chem.*, 2016, **774**, 102–110.
49 O. Kasian, S. Geiger, K. J. J. Mayrhofer and S. Cherevko, *Chem. Rec.*, 2019, **19**, 2130–2142.
50 F. Zeng, C. Mebrahtu, L. Liao, A. K. Beine and R. Palkovits, *J. Energy Chem.*, 2022, **69**, 301–329.
51 P. Jovanovič, N. Hodnik, F. Ruiz-Zepeda, I. Arčon, B. Jozinović, M. Zorko, M. Bele, M. Šala, V. S. Šelih, S. Hočevar and M. Gaberšček, *J. Am. Chem. Soc.*, 2017, **139**, 12837–12846.

